JOURNAL OF SPACECRAFT AND ROCKETS
Vol. 30, No. 2, March–April 1993

Heatshield Erosion in a Dusty Martian Atmosphere

Periklis Papadopoulos*
Stanford University, Stanford, California 94305
Michael E. Tauber†
NASA Ames Research Center, Moffett Field, California 94035
and
I-Dee Chang‡
Stanford University, Stanford, California 94305

The effects of dust particle impacts on the erosion of the forebody heatshield were calculated for a 26 m diameter aerobraking vehicle entering a dusty Martian atmosphere at 8600 m/s. An explicit, thin-layer, Navier-Stokes code was used to compute the dustless flowfield about the vehicle for the actual Martian atmospheric composition. The deceleration and melting of 1–19μm diameter dust particles within the forebody shock layer were computed. All particles began vaporizing shortly after entering the shock layer, but most survived to hit the heatshield surface. The two different heatshield materials considered were Shuttle ceramic tiles and the ablator used on the Apollo capsule. For a vehicle with a ballistic coefficient of 200 kg/m^2, the heatshield surfaces experienced an average of about 7 mm of surface erosion. For the ablator, the increase in the forebody thermal protection mass was 29%, or about 1.3% of the vehicle's mass. This modest mass penalty does not compromise the use of aerobraking at Mars.

Nomenclature

A = reference area of entry vehicle, m^2
a = particle's surface accommodation coefficient
C = constant, Eq. 4
C_D = drag coefficient
c = specific heat of the particle, J/kgK
D = drag
D_c = impact crater diameter, m
d_p = particle, or projectile, diameter, m
e = total energy per unit volume, J/m^3
e_{int} = internal energy per unit mass, J/kg
F_m = mass fraction (see Fig. 1)
h = average heat-transfer coefficient, W/m^{2}K
h_{st} = static enthalpy, J/kg
k = coefficient of thermal conductivity, W/mK
KE_p = particle, or projectile, kinetic energy
L = lift
M = Mach number of particle in shock layer, based on ΔV
m = vehicle mass, kg
$\hat{m}$ = mass loading of particles
$\bar{m}$ = mass area density, kg/m^2
m_p = particle, or projectile, mass, kg
N = total number of particles per unit area encountered during aerobraking, m^{-2}
Nu = Nusselt number
P = pressure, N/m^2
Pr = Prandtl number
P_v = vaporization pressure, N/m^2
p = surface penetration, m
$\dot{q}_{\text{av}}$ = average heat transfer rate, W/m^2
Re = Reynolds number based on particle diameter
Rn = vehicle nose radius, m
r = mean particle radius, m
r_m = "mode" radius, m
r_p = dust particle radius, m
s = distance along flight path, m
T = temperature of the gas in the shock layer, K
T_p = temperature of the particle, K
T_v = vaporization temperature of the particle, K
T_w = vehicle wall temperature, K
u = x component of local flow velocity, m/s
v = y component of local flow velocity, m/s
V = flight velocity, m/s
V_E = atmospheric entry velocity, m/s
V_p = particle, or projectile, velocity, m/s
V_{SK} = skip-out velocity, m/s
α = angle of attack
β = real-gas equation of state parameter
γ = effective specific heat ratio
ΔV = relative velocity between the particle and the gas, m/s
ζ = specific heat of vaporization, J/kg
θ = angle between particle velocity vector at impact and the normal to the surface
ρ = local flow density, kg/m^3
ρ_p = density of the particle, kg/m^3
ρ_∞ = freestream density, kg/m^3
τ = optical depth, m

Presented as Paper 92-0855 at the AIAA 30th Aerospace Sciences Meeting, Reno, NV, Jan. 6–9, 1992; received Jan. 13, 1992; revision received Aug, 3, 1992; accepted for publication Sept. 21, 1992.

*Graduate Student, Department of Aeronautics and Astronautics. Member AIAA.
†Research Scientist, MS 229-3; also, Lecturer, Department of Aeronautics and Astronautics, Stanford University. Associate Fellow AIAA.
‡Professor, Department of Aeronautics and Astronautics. Member AIAA.

Introduction

IN May 1990, the President announced an initiative for space exploration that is to culminate in landing men on Mars in approximately 20 years. Numerous Mars mission studies that were made in the past 25 years[1–5] have shown that large weight savings can be achieved by using atmospheric braking instead of decelerating propulsively. Early missions will likely be the planetary opposition type, which last 14 to 16 months and have shorter trip times to maximize the safety of the crew.[6] In contrast with the 2 to 3 year-long conjunction missions, these shorter trip times result in somewhat higher

entry velocities at Mars, thus requiring the vehicle to have more heatshielding.

The structure of the Martian atmosphere[7] and its composition[8] are known. However, it has also been observed[9-12] that dust particles are present to high altitudes in the Martian atmosphere. In fact, during or after a major dust storm, the dust extends to altitudes beyond 35–50 km where aerobraking maneuvers will be performed.[13-15] Small dust particles are present even under quiescent conditions in the Mars atmosphere, and the concentration increases by an order of magnitude when major dust storms occur. A vehicle arriving at Mars is faced with the possibility of having to aerocapture in a dust-laden atmosphere. Therefore, the vehicles must have heatshields that are designed to withstand the erosion that is produced by dust particles that are suspended in the atmosphere to high altitudes as a result of major dust storms.

The objectives of this paper are to present the results of calculations that have been made to determine the extent of the forebody heatshield erosion from dust particle impacts that occur on a large, blunt, low lift/drag (L/D) ratio aerobrake configuration. Initial estimates of heatshield erosion, based on calculations made at one point in an aerobraking trajectory and for one dust particle size, were published by the authors.[16] In the present paper, the calculations of Ref. 16 are extended to 1) finding where in the entry corridor the heatshield dust erosion is at a maximum, 2) computing the erosion at many more points in the trajectory, and 3) using a distribution of dust particle sizes. An inertial reference entry velocity of 8600 m/s has been used; the relative entry velocity with respect to the rotating Martian atmosphere is 8400 m/s. This velocity is near the upper limit that has been considered for manned missions. The flowfield about a 26 m diam vehicle is computed at representative flight conditions using the actual Mars atmospheric composition. The paths, deceleration, heating, and sublimation of dust particles that enter the shock layer at various locations are calculated and traced to surface impact. Since the surface erosion is proportional to the number, size, and velocity of the impacting particles, these parameters are determined as a function of forebody location. Two heatshield materials are considered. The first one has a glass surface and is representative of the radiatively cooled hot surface, backed by insulative material, construction that is used for the Shuttle tiles. The second one is a low-temperature, medium-density (545 kg/m^3) ablator known as AVCOAT-5026. The approximate amount of both local and total ablator removed by dust erosion will be calculated. In addition, a scaling relation is derived to permit extrapolating the results to vehicles that have similar shapes and sizes, but have different entry velocities and ballistic coefficients.

Before proceeding, it is essential to estimate the likelihood of encountering a heavily dust-laden atmosphere. The focus here is on global dust storms, as opposed to the frequent, but short-lived, local ones. At least six and possibly eight global dust storms were observed at Mars from 1956 through 1982.[17-19] If the global dust storm activity during that 26-year period is assumed to be representative, then there is a probability of averaging one global dust storm every 3.3 to 4.3 (Earth) years. However, global storms do not happen at regular intervals. For example, two major storms occurred in 1977. These events provided the Viking landers with opportunities for gathering data of the atmospheric residence time of the dust.[17,18] By measuring the absorption of solar radiation, which is increased when dust is present, it was found that the dust concentration reached its peak about 20 days after the beginning of the storm. The dust level decreased to the prestorm value within about three months. The distribution of dust particle sizes was deduced from two independent measurements[9,10] that will be briefly described later. However, there is no data on how long the larger particles (5–10 μm diam) that cause most of the heatshield erosion (as will be shown later) remain suspended in the region of the atmosphere where aerocapture occurs. In the absence of large-scale vertical atmospheric circulation, 10 μm particles would settle to low altitudes within days, for example. However, dust storms are, obviously, accompanied by strong vertical winds, or the dust would not reach the 50–60 km altitudes at which it was observed from orbit.[12] Therefore, a lower value of 20 days (the time to reach maximum solar flux obscuration) and an upper value of 50 days (half the duration of the observed solar flux reduction) have been chosen to estimate the residence time of large dust particles. These values result in a probability of encountering large dust particles during aerocapture of about 2–4% of the time. This probability is high enough so that provisions for dust-caused erosion of the heatshield must be included in the design of the vehicle.

Analysis

The shock-layer flowfield surrounding the body is calculated by using an explicit, finite-difference, shock-capturing algorithm for viscous hypersonic flows in thermochemical equilibrium.[20] The dustless flowfield is computed using the actual Martian atmospheric composition. The deceleration, heating, and vaporization of the dust particles within the shock layer are calculated, subsequently, in an uncoupled manner. The dust particles' trajectories are traced until they either vaporize completely or hit the vehicle's surface. First the flowfield solution method is discussed. Next the atmospheric environment is described. This is followed by a description of the computation of the particles' trajectories and heating within the shock layer and a discussion of hypervelocity impacts into the heatshield materials considered here. Discussion of those topics that were previously covered in more detail[16] will be abbreviated here.

Chemistry Modeling

The actual Martian atmospheric composition[8] consisting of 95.5% CO_2, 1.6% Ar, 2.7% N_2, 0.13% O_2, and 0.07% CO is used. The real-gas equation of state can be written as

$$P = (\beta - 1)[e - 0.5\rho(u^2 + v^2)] \tag{1}$$

where β is the ratio of static enthalpy to internal energy

$$\beta = h_{st}/e_{int} = h_{st}/(h_{st} - P/\rho) \tag{2}$$

at a reference value of temperature of 298.15 K.

The equilibrium state of the gas at each grid point is determined by minimizing the Gibbs free energy subject to conservation of mass and static enthalpy. This procedure is performed within the chemistry routine.[21] A Newton-Raphson method is used to solve the system of nonlinear equations. The iteration procedure is continued until the system converges.

The inputs to the chemistry routine are values of enthalpy, entropy, and specific heat for each chemical species and are obtained as follows. From 300–6000 K, the values are obtained from JANAF tables. For higher temperatures (6000–7000 K), values based on an extrapolation of the JANAF data[21] are used.

The species considered are CO_2, N_2, Ar, O_2, CO, N, C, NO, CN, e^-, and O. The output of the chemistry routine includes the equilibrium values of temperature, molar mass, density, and β, where β is defined by Eq. (2).

Flowfield Computation

The steep gradients occurring in the flow properties across strong shocks associated with hypervelocity flow computations can cause numerical stability problems. Flux limiters are used to control the instabilities across the shock. In the present computation, flux vector splitting with upwind differencing is employed. The flowfield solution procedure is described in detail in Ref. 20.

The two-dimensional, or axisymmetric, Navier-Stokes equations for a gas in thermochemical equilibrium were solved using a combination of a second-order and first-order upwind

differencing algorithm. The Steger-Warming flux-splitting technique was used and differencing was performed according to the direction of signal propagation. However, these split fluxes are not continuously differentiable through the sonic points. Therefore, a small correction parameter ϵ was used to modify the eigenvalues, $\lambda_i = \pm \frac{1}{2}(\lambda_i \pm \sqrt{\lambda_i^2 + \epsilon})$, and to smooth out the discontinuity, thus preventing oscillation of the solution.[20] Second-order upwind differencing is used throughout the shock layer to resolve the viscous boundary layer. Through the shock, first-order differencing is used since second-order differencing through a discontinuity induces oscillations in the flowfield solution. The use of the first-order method through the shock, however, produces some inaccuracies and shock smearing, but this can be minimized by grid restructuring. The use of grid restructuring will be discussed later.

The governing equations are transformed to a generalized coordinate system (ξ,η). Consistent with the thin-layer approximations for the viscous terms, only the viscous derivatives normal to the wall (η) are considered. Freestream values are used for the boundary conditions ahead of the shock. Along the body surface, a nonslip flow condition is enforced, and realistic wall temperatures are specified. A time step corresponding to a maximum Courant-Friedrichs-Lewy (CFL) number of 0.49 was used.

The three-dimensional blunt aerobrake configuration is approximated by using an axially symmetric body. Therefore, it was only necessary to compute the flow in a plane of symmetry, thus reducing the computation time by an order of magnitude. The hypervelocity flow features, such as the shock wave, the viscous boundary layer, and the expansion about the corner of the vehicle, are resolved using a self-adaptive grid method. An initial flow solution is used, and the grid points are then redistributed in strong gradient regions. A new solution is then computed using the adapted grid, thus resulting in a more accurate flowfield computation by minimizing grid error. In the self-adaptive grid procedure that is used,[22] the two-dimensional grid adaption problem is split into a series of one-dimensional problems. The principle is analogous to applying tension and torsion spring forces that are proportional to the local flow gradients at every grid point and determining the resulting grid point distribution by calculating the equilibrium state of the system. The grid adaption was essential in restructuring the grid points of the vehicle geometry to minimize both the local and overall numerical errors.

The free-energy minimization technique discussed earlier is coupled with the gasdynamics to compute the chemical equilibrium of this complex system. The state of the system is specified by assigning two thermodynamic properties. Static enthalpy and pressure are held constant during the Gibbs free-energy minimization.

Dust Environment

Observations of the Martian sky and the sun during the two Viking missions using both orbiter and lander imaging instruments were used to infer atmospheric dynamics and properties of the dust suspended in the atmosphere. The winds on Mars frequently exceed the threshold value for setting the dust particles into motion and short-lived local dust storms occur frequently. The presence of dust in the atmosphere has a significant effect on the vertical and horizontal atmospheric temperature gradients and thus also affects the atmospheric dynamics. Although a threshold value of winds is required to set the dust into motion, its presence in the atmosphere also affects the wind intensity. Thus, there exists a feedback system between dust loading and the ability of the winds to raise more dust. This feedback is positive for optical depth of less than 1.25 and negative for larger values of optical depth. Dust loading is related to optical depth through the following equation:

$$\hat{m} = (\tfrac{2}{3})r\rho_p\tau \qquad (3)$$

Although the aforementioned feedback system has been identified, there are other less well understood factors controlling the development of dust storms. It has been hypothesized[9] that perhaps the Martian atmospheric pressure is just barely large enough for the development of global dust storms. This hypothesis is based on the observation that global dust storms occur at times close to perihelion, when the wind speeds may increase with increasing insolation, and that the optical depth of global dust storm development is very close to the boundary between positive and negative dust-wind feedback.

During the Viking missions, two global dust storms were observed. At the onset of the storms, a very rapid rise in the opacity of the atmosphere was observed.[18] Observations of these dust storms provide evidence that local dust storms can expand into global dust storms and that, once this expansion begins, it proceeds very rapidly, reaching mean meridional velocities up to 30 m/s.

Observations during the dust storms were performed with several imagers, and solar opacity measurements from the landers' cameras provided valuable information of dust particle sizes. In addition to the Viking landers' ground-based measurements, much information about particle sizes and composition was deduced from the infrared interferometric spectrometers on board the Mariner 9 orbiter (1971 storm) and the Viking orbiter (1977 storms). The Mariner 9 data were extensively analyzed in Ref. 10 where a particle size distribution was derived. The resulting modified gamma distribution[10] has the form

$$\bar{N}(r) = C\, r_p^2 \exp[-4(r_p/r_m)^{1/2}] \qquad (4)$$

where a value of the mode radius r_m of 0.4 (10^{-6}) m has been used. As is to be expected from Eq. (4), the most abundant particles have diameters of 0.8 μm. However, when the mass-averaged size distribution is calculated using Eq. (4), and the normalized mass fractions are plotted (see Fig. 1), the mean-mass particle diameter becomes 5 μm whereas particles that are 1 μm or less in size contribute negligibly. The 5 μm mean-mass size was also deduced from both the ground- and space-based measurements.[9,10] For simplicity, 5 μm diam particles were used in the heatshield erosion calculations previously reported.[16] In contrast, the size distribution shown in Fig. 1 will be employed in the present calculations. The particle shape and composition were also deduced[10] from the data. The particles' shapes were deduced to be plate-like. However, because the particle orientation will be random and to simplify the present calculations, a spherical shape will be used. The composition of the particles was found to be clay-like, consist-

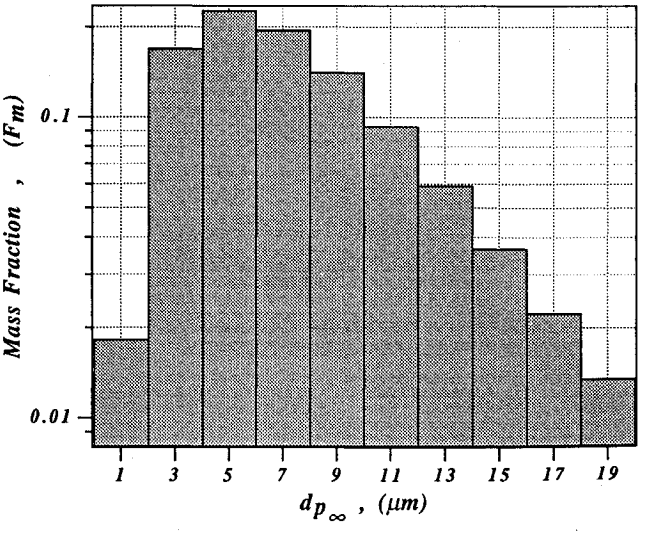

Fig. 1 Dust particle mass fractions.

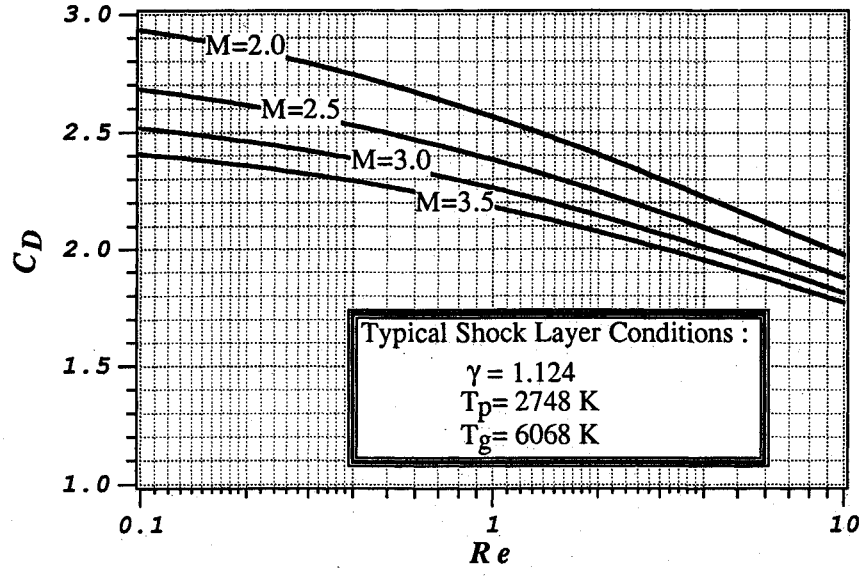

Fig. 2 Drag coefficient vs Reynolds number.

ing primarily of Montmorillonite and some basalt. The primary constituent, about 70%, is SiO_2, with 15–20% being Al_2O_3 and a few percent of iron oxides, among other trace compounds, being present.

The vertical distribution of dust particles in the atmosphere was also inferred from both ground-based and satellite-based light absorption measurements and upper atmospheric temperatures.[9-11,18] From these data it was inferred that during a major dust storm and for some period (of at least weeks) after the peak intensity of the event, the dust was uniformly mixed within the atmosphere. The dust extended to an altitude of at least 40 km, and the mass-mixing ratio was about 10^{-4}. That is, the ratio of dust mass per unit volume to ambient atmospheric gas mass per unit volume was 10^{-4}, and this ratio remained constant to an altitude of at least 40 km. For lack of more definitive mass-mixing data, the mixing ratio of 10^{-4} will be used here to altitudes as high as 56 km. However, most of the aerocapture maneuver occurs at altitudes very close to 40 km, as will be shown subsequently.

Dust Particle Tracing

The dust particles encountered by the vehicle move through the shock layer with a velocity that is different from that of the local flowfield. The drag and heat transfer experienced by the particles are determined by the relative velocity between the particles and the flow velocity, which is found numerically. The effect of the dust particles on the shock-layer flowfield is neglected, thus permitting the uncoupling of the flowfield and particle motion computation. This assumption should be valid for the very small mass-mixing ratios of 10^{-4} encountered here.

The dust particle motion is governed by the conservation equations of momentum, mass, and energy. By combining the expression for aerodynamic drag with Newton's second law of motion, it can be shown that the equation of motion of a spherical particle in the shock layer is

$$\frac{dV_p}{dt} = \frac{3}{8}\left(\frac{\rho}{\rho_p}\right)\left(\frac{C_D}{r_p}\right)(\Delta V)^2 \tag{5}$$

Although opacity measurements indicate that the dust particles may have plate-like shapes, here it is assumed that the particles are spherical. This is considered to be a reasonable assumption for modeling the interaction of the dust particles with the flowfield since the particles will tend to have a random orientation.

The trajectories and heating of particles in a hypersonic shock layer have been formulated previously.[23] However, the nature of the shock-layer flow in which the particles are immersed is very different here from that discussed in Ref. 23. In Ref. 23, the Reynolds numbers of the particles are on the order of 1000 or greater. Therefore, the particles experience continuum flow and are assumed to have a constant C_D of about one, at relative supersonic speeds. In contrast, the dust particles being studied here, typically, have Reynolds numbers based on particle diameter, of about one and are in the transitional or free-molecular flow regime. In these rarified flows, the drag coefficients can be much higher than in continuum flow.

The drag coefficient correlation[24] that is used in evaluating Eq. (5) covers a wide range of conditions applicable to continuum, transitional, and free-molecular flow regimes.[25] The correlation incorporates the effect of a temperature difference between the spherical particle and the gas and includes particle Reynolds number and Mach number based on relative velocities. An example calculation for the drag coefficients of spherical dust particles at relative Mach numbers from 2 to 3.5, within the vehicle's shock layer, is shown in Fig. 2. The C_D values vary from about 1.8 to 2.9 over the Reynolds number range from 10 to 0.1, respectively; these drag coefficients are much higher than the continuum flow values.

As the dust particles enter the hot shock layer surrounding the vehicle's forebody, they are rapidly heated. Once the particle's surface temperature reaches the sublimation value, the surface vaporizes and the particle will shrink in size as it traverses the shock layer. If the particle's initial size is sufficiently small, it may vaporize before hitting the heatshield or become so small that it may follow the flow streamlines and not hit the vehicle's surface. Therefore, for large vehicles such as the one being considered here that have thick shock layers, the sublimation of the particles must be considered.

The dust particles are sufficiently small to experience rarefied or at times free-molecular flow within the shock layer of the blunt body. The heat transfer to the dust particles will be computed using the following rarefied flow expression[26]:

$$\frac{Nu^0}{Nu} = 1 + \frac{(2\pi\gamma^3)^{1/2}}{\gamma+1}\left(\frac{2-a}{a}\right)\frac{M}{Re\,Pr}\,Nu^0 \tag{6}$$

where Nu is defined as

$$Nu = \frac{h\,d_p}{k} \tag{7}$$

An accommodation coefficient of 0.9 was used in the computations.[27] In Eq. (6),

$$Nu^0 = 2 + 0.459\,Re^{0.55}\,Pr^{0.33}$$

The heat transfer that is computed from Eq. (6) is shown in Fig. 3 and compared with other computations and empirical fits to data.[27] The agreement is reasonably good considering the complexity of the phenomena that are being modeled. Note that the Nusselt numbers (heating rates) are much lower in rarefied flow than in continuum flow. Only the convective heating of the particles has been considered. The heating of the particles by shock-layer radiation from the two most prominent radiators, the CO(4 +) and CN molecules, was calculated but found to be negligible.

The surface temperature of the particles is found from the following expression[28]:

$$\frac{dT_p}{dt} = \frac{6h}{\rho_p c d_p}(T - T_p) \tag{8}$$

The sublimation temperature relation for SiO_2, glassy material, is[29]

$$T_v = \frac{57400}{18.5 - \ell n P_v} \tag{9}$$

For typical conditions of interest here, T_v is about 2600–2700 K. When the particle's surface temperature reaches the vaporization temperature, the particle size shrinks. The rate of change of the particle diameter can be written as

$$\frac{dr_p}{dt} = \frac{1}{2\rho_p}\left(\frac{\dot{q}_{av}}{\zeta}\right) \tag{10}$$

where ζ is given[30] as 8.6×10^6 J/kg.

Equations (5), (6), (8), and (10) form a mildly stiff system of four ordinary differential equations. A multistep Runge-Kutta formulation is used to solve this initial-value problem. The technique used is a one-step integrator that advances the solution a single step in the direction of dust particle velocity and is iterated until convergence is reached. The time step is controlled by the integrator. The integration is terminated when the particle vaporizes completely or hits the vehicle surface.

Hypervelocity Impact Phenomena

The determination of cratering of surfaces that are subjected to hypervelocity impacts still defies precise theoretical analysis. The complexity of the problem is due to the many factors that affect the size and shape of the craters. Although it has long been known that the kinetic energy of the impacting projectile is the most important factor,[31] other parameters such as the composition, density, and strength of both the target and the projectile, in addition to the shape and size of the projectile, can have a major influence. This multiplicity of parameters has made it necessary to treat the impact damage phenomenon empirically.[32,33] Since the derivation of the microcratering relations that will be used here has been presented previously,[16] only an abbreviated version will be given.

Since the impacting dust particles are composed primarily of silicates, it is assumed that experimental data using small, spherical, Pyrex glass projectiles can be used to represent the impact effects created by the dust particles. Two different heatshield materials are considered, based on previous entry heatshielding calculations.[14] For entry velocities up to 8600 m/s, it was found that vehicles having ballistic coefficients in the vicinity of 100 kg/m^2, or less, can be radiatively cooled if the heatshield surface has a high emissivity and inhibits atomic and molecular recombination. Therefore, a Shuttle tile refractory material, such as FRCI-12, (192 kg/m^3), was considered. The tile's tetraborosilicate, black, glass surface is essential to achieve a high emissivity (0.8–0.9) and also inhibits surface reactions. This surface glass layer is about 0.35 mm thick. Below the glass surface is the low-density silicate insulation that is structurally much weaker. For lack of data on a more representative material, the surface impact damage was modeled by using experiments performed on glass slab targets. For vehicle ballistic coefficients of 200 kg/m^2 and greater, the heating rates exceeded 100 W/cm^2 over most of the forebody, thus requiring an ablative heatshield. The ablator that is considered here is AVCOAT-5026, a medium density, epoxy resin impregnated, silicaceous material that was used on the Apollo capsule for lunar return.

During the Apollo project, concern about micrometeoroid damage to windows led to simulation and studies of hypervelocity impact into glass slabs. The experiments that were performed yielded valuable information on the dimensions and shapes of craters produced in glass as a function of projectile size and velocity.[34] For spherical projectile diameters of 0.4 to 1.6 mm, the velocities ranged from about 250 to 7000 m/s. The data were fit empirically based on the assumption that crater diameter is proportional to the kinetic energy of the projectile to the one-third power. (This scaling relationship

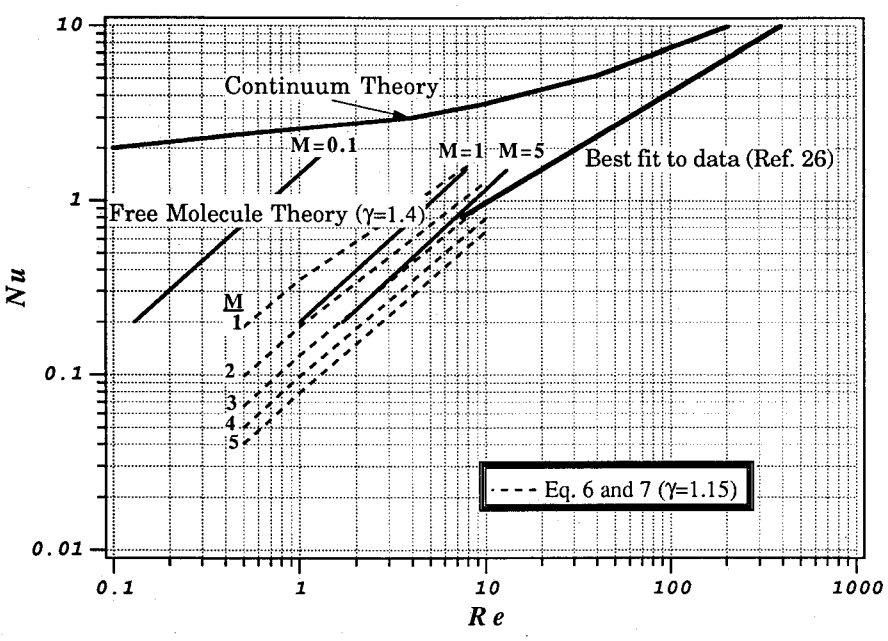

Fig. 3 Nusselt number vs Reynolds number.

appears to be approximately valid over many orders of magnitude in energy, from micro- to macrocraters).[35] The expressions that were derived and will be used to predict the ratios of crater diameter and depth to projectile diameter in glass are, respectively,

$$D_c/d_p = 0.113 V_p^{0.667} \tag{11}$$

and

$$p/d_p = 0.3016 d_p^{0.4} V_p^{0.667} \tag{12}$$

The crater depth produced in virgin AVCOAT ablator by impacting small glass projectiles was determined empirically[36] and is given as

$$p/d_p = 0.0346(d_p)^{0.06} V_p^{0.667} \tag{13}$$

However, Eq. (13) is not valid when the surface is ablating. To approximately account for the greater damage that will occur to the low-density charred surface material during ablation,[37] the crater depth given by Eq. (13) has been increased by applying inverse density scaling. (The density of the char is about one-half that of the virgin ablator, and this ratio was raised to the -0.6 power.) In view of the uncertainty of the material's response during ablation, keeping the extremely weak dependence on particle size on the right-hand side of Eq. (13) is not warranted. An impacting particle size of 3 μm was used in Eq. (13) to arrive at the following expression that will be used here:

$$p/d_p = 0.024 V_p^{0.667} \tag{14}$$

Since no information could be found to determine crater-to-projectile diameter ratios for either virgin or ablating AVCOAT, it was assumed that the crater had a hemispherical shape. In that case, $D_c = 2p$, which gives

$$D_c/d_p = 0.048 V_p^{0.667} \tag{15}$$

The number of dust particles per unit area that the vehicle encounters during an aerobraking pass are found by integrating the atmospheric mass density along the trajectory and multiplying the result by the ratio of particle density to atmospheric density. Assuming that the dust mixing ratio is independent of attitude and using a value of 10^{-4} for major dust storm conditions leads to

$$N = (10^{-4}/\Sigma F_m m_p) \int \rho_\infty \, ds \tag{16}$$

The size and velocity of the dust particles at the time of impact on the vehicle's surface is found from the flowfield/particle interaction computation. Knowing particle size and velocity vector at impact permits evaluation of the crater

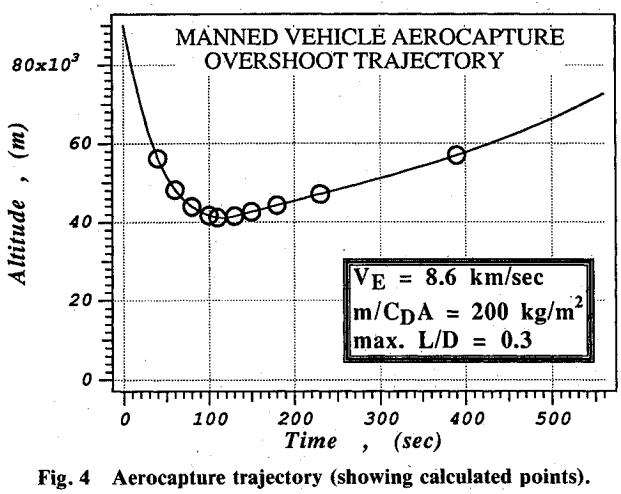

Fig. 4 Aerocapture trajectory (showing calculated points).

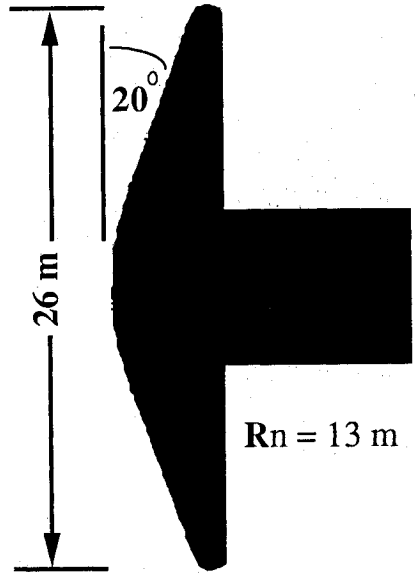

Fig. 5 Vehicle geometry used for calculations.

depths and diameters. Combining knowledge of the shape, area, and depth of each crater with the number of impacts per unit area leads to the local surface erosion depth, Σp, where

$$\Sigma p \sim D_c^2 p N (\cos\theta)^n \tag{17}$$

In Eq. (17), the cosine term is used as a geometric factor at impact and is also used to estimate the effect of multiple, sequential impacts, since crater depths in the same area are not directly additive, usually. For example, once a crater is formed, it is probable that subsequent impacts will occur nearer the edge of the original crater rather than at its center where the depth is greatest. For the shallow craters that are formed in glass, $n \ll 1$, whereas for the assumed hemispherical crater shapes in AVCOAT, $\theta = 45$ deg and $n = 1$ were used. The preceeding values for n and θ were chosen to be somewhat conservative since more precise numbers could not be found.

Results

In the results that will be presented here, it has been assumed that the influence of the dust particles on the shock-layer flow can be neglected. The decoupling of the particle computation from that of the flowfield greatly simplifies the formulation of the problem and speeds convergence. The rationale for the decoupling is based on the low particle density to freestream density ratio of 10^{-4}; within the forebody shock layer, the ratio decreases to about $5(10)^{-6}$, or roughly 10^6 dust particles/m^3. Therefore, the flowfield computations to be shown will be for a dustless Martian atmosphere. The effect of the shock-layer flow on the deceleration, heating, and melting of the dust particles at various body locations will be illustrated. Knowing the dust particles' sizes and velocities at heatshield surface impact enables the estimation of surface erosion.

Vehicle Aerocapture Trajectory

The results of the computations to be shown were made for one aerocapture trajectory. The entry velocity relative to the rotating atmosphere was 8400 m/s, the vehicle's maximum L/D was 0.3, and lift modulation was used. The ballistic coefficient was taken to be 200 kg/m^2. A trajectory near the upper, or overshoot, boundary of the entry corridor was chosen, primarily since the erosion was found to be more severe than near the lower, or undershoot, boundary. (If the dust particle size distribution is assumed to be independent of altitude as was done here, then essentially the same total

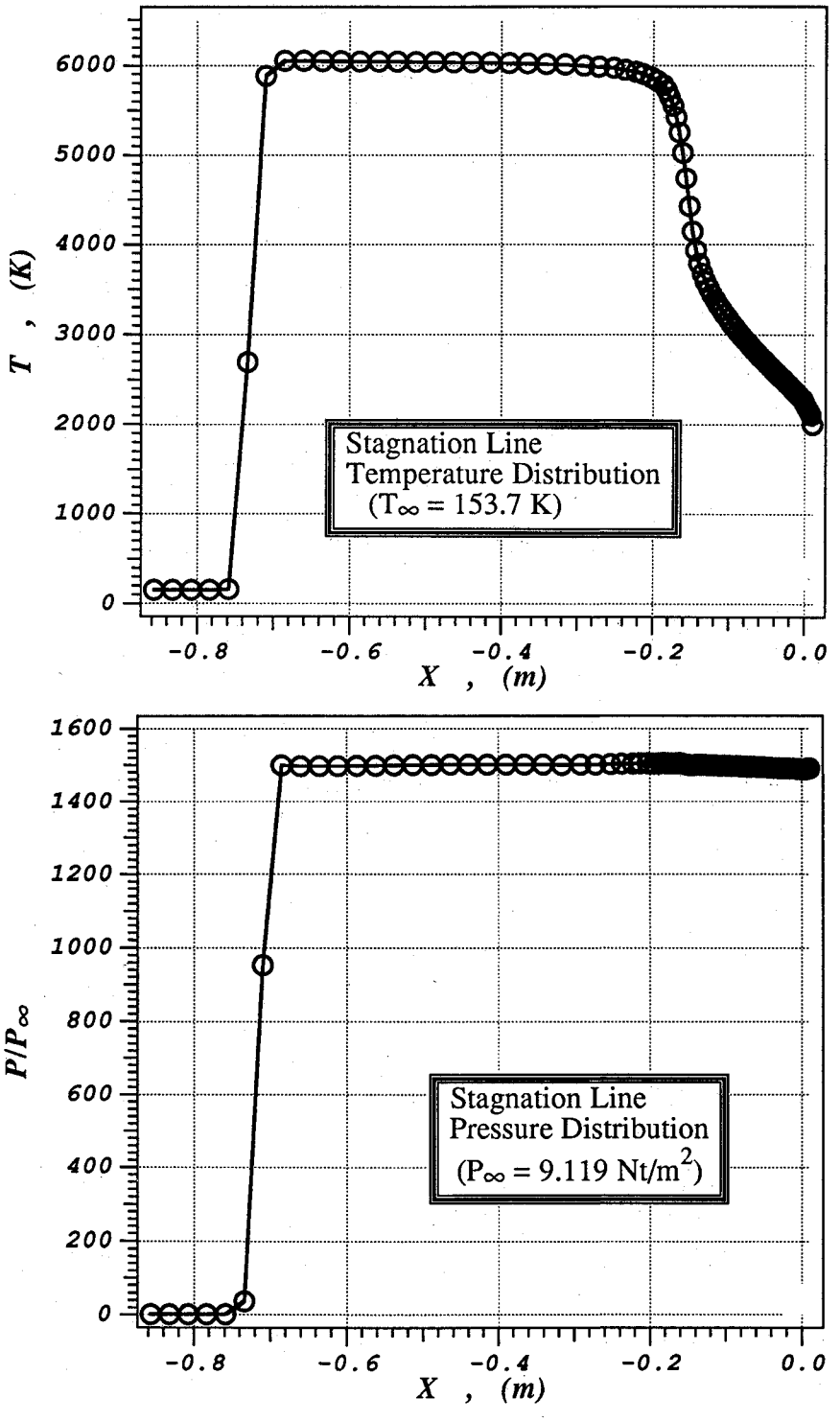

Fig. 6 Flow properties on stagnation streamline (altitude = 41.65 km, V_∞ = 6831 m/s): a) temperature, b) pressure, and c) density.

number of particles are encountered along all trajectories within the flight corridor. However, the vehicle's shock-layer gas density is lowest at overshoot so that the dust particles are decelerated and heated less and hit the surface more energetically.) The trajectory that was used is illustrated in Fig. 4. Also shown in Fig. 4 are the 10 points along the trajectory where the heatshield erosion was calculated. The 10 points span altitudes from 41 to 56 km with 5 points being below 45 km where the greatest numbers of particles were encountered.

Dustless Flowfield

The flowfield about the body was computed at zero angle of attack. The configuration was a 70 deg half-angle cone with a nose radius equal to the body radius that was 13 m (see Fig. 5). The axisymmetric flow about the body was computed using a 106 × 64 grid. Thermodynamic and chemical equilibrium were assumed; this assumption is valid, especially below 50 km, because of the large size of the vehicle. The forebody flowfield solution was well converged after 35 min of CPU time using a CRAY-YMP computer. Along the windward surface of the vehicle, the wall temperature was assumed to be invariant with location, but the temperature was varied as a function of heating rate along the trajectory. A maximum wall temperature of 2000 K was, somewhat arbitrarily, chosen since that value was between the surface temperatures of ceramic tiles and the ablator, AVCOAT. (The heatshield erosion results to

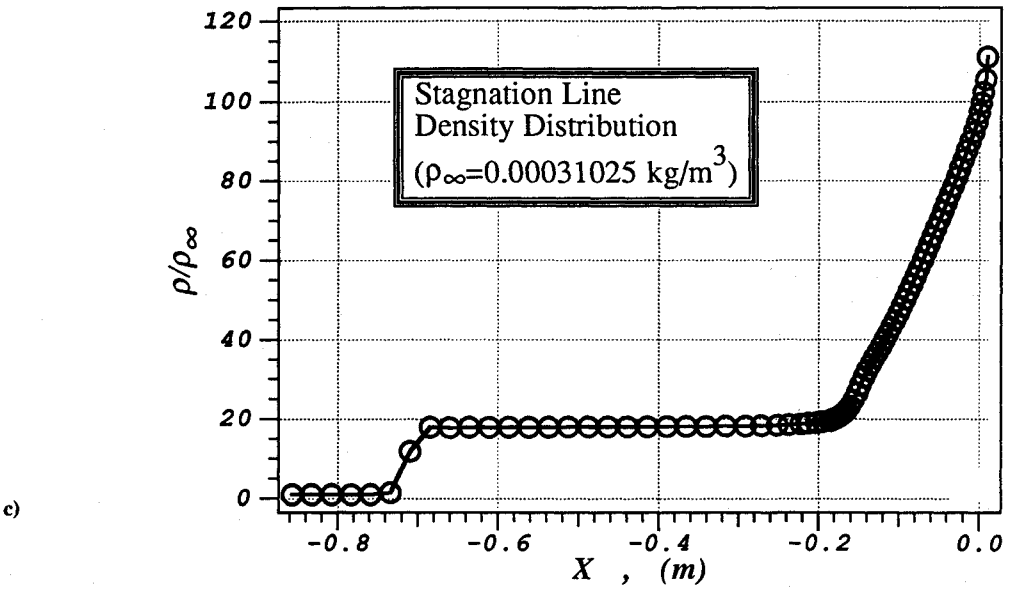

Fig. 6 (cont.) Flow properties on stagnation streamline (altitude = 41.65 km, V_∞ = 6831 m/s): a) temperature, b) pressure, and c) density.

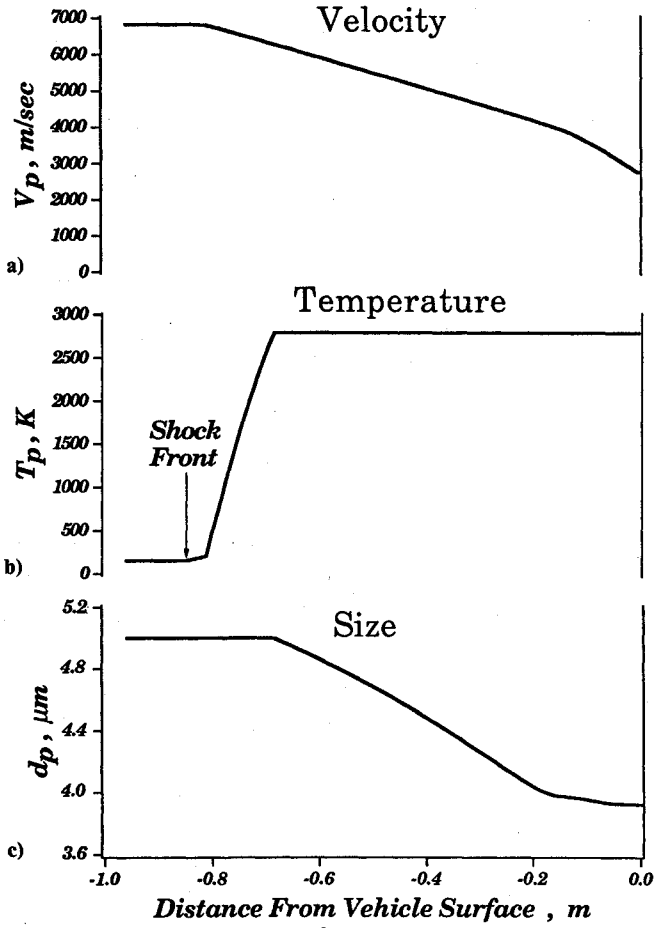

Fig. 7 Particle tracing 4 m from stagnation point: a) velocity, b) temperature, and c) size.

be presented are not sensitive to moderate variations in wall temperature, such as ± 500 K.)

An example calculation of a portion of the forebody flowfield is shown at a flight velocity of 6810 m/s and altitude of 41.65 km. The stagnation line flowfield properties of temperature, pressure ratio, and density ratio for this case are shown in Fig. 6. The shock standoff distance on the stagnation streamline is about 0.73 m. In the inviscid region of the shock layer, the density jump across the shock is about 18. Note that the laminar boundary layer occupies about 25% of the shock layer for this case where a 2000 K wall temperature was used. A laminar boundary layer has been assumed throughout. (In reality, it is very likely that transition to turbulence would occur on the forebody and that the boundary layer would be fully turbulent in the vicinity of the shoulder. Since most of the deceleration and heating of the dust particles occur in the inviscid part of the shock layer, the state of the boundary layer should not have a major influence.) The behavior of dust particles within the shock layer, at the aforementioned point in the trajectory, will be discussed next.

Dust Particles in Shock-Layer

The conditions experienced by a dust particle, which has an initial diameter of 5 μm and enters the shock layer at a location that is a radial distance of about 4 m from the stagnation line, will be illustrated. The particle experiences rarefied flow within the shock layer and has a Reynolds number of about 0.6 at M = 3.5. The resulting drag coefficient is about 2.25, causing the particle to decelerate to 40% of its initial velocity at surface impact, as can be seen in Fig. 7a. The surface temperature of the particle is shown in Fig. 7b. About 15 cm beyond the shock, the vaporization temperature is reached and the particle continues to sublimate as it moves toward the wall (see Fig. 7c). At surface impact, its size has decreased by 22%. Therefore, the kinetic energy of the example particle has been reduced to about 8% of its initial value by shock-layer gas drag and heating. Since the hypervelocity impact crater depth is proportional to the kinetic energy to the one-third power for many materials, the shock-layer/particle interaction reduces the surface erosion to less than one-half the value that would be found if the particle deceleration and vaporization in the shock layer were ignored.

The effect of the initial sizes of the particles and where they enter the shock layer is considered next. Initial particle diameters ranging from 1 to 19 μm, in increments of 2 μm, were considered and radial distances ranged from the stagnation point to 12 m, or near the vehicle's shoulder. Examples of sizes and velocities of the particles at surface impact are shown in Fig. 8, for two particles having initial diameters of 5 and 7 μm and for all 10 points along the vehicle's trajectory. Since the shock-layer thickness more than doubles in going from the stagnation point region to the vehicle's shoulder, small particles entering the shock layer at large radial distances can vaporize completely before hitting the surface. In contrast, particles that are initially 5 μm, or larger, will still hit the surface, although all but the largest ones will have been strongly decelerated. Note also from Fig. 8 that at flight velocities below about 6000 m/s for an aerocapture trajectory,

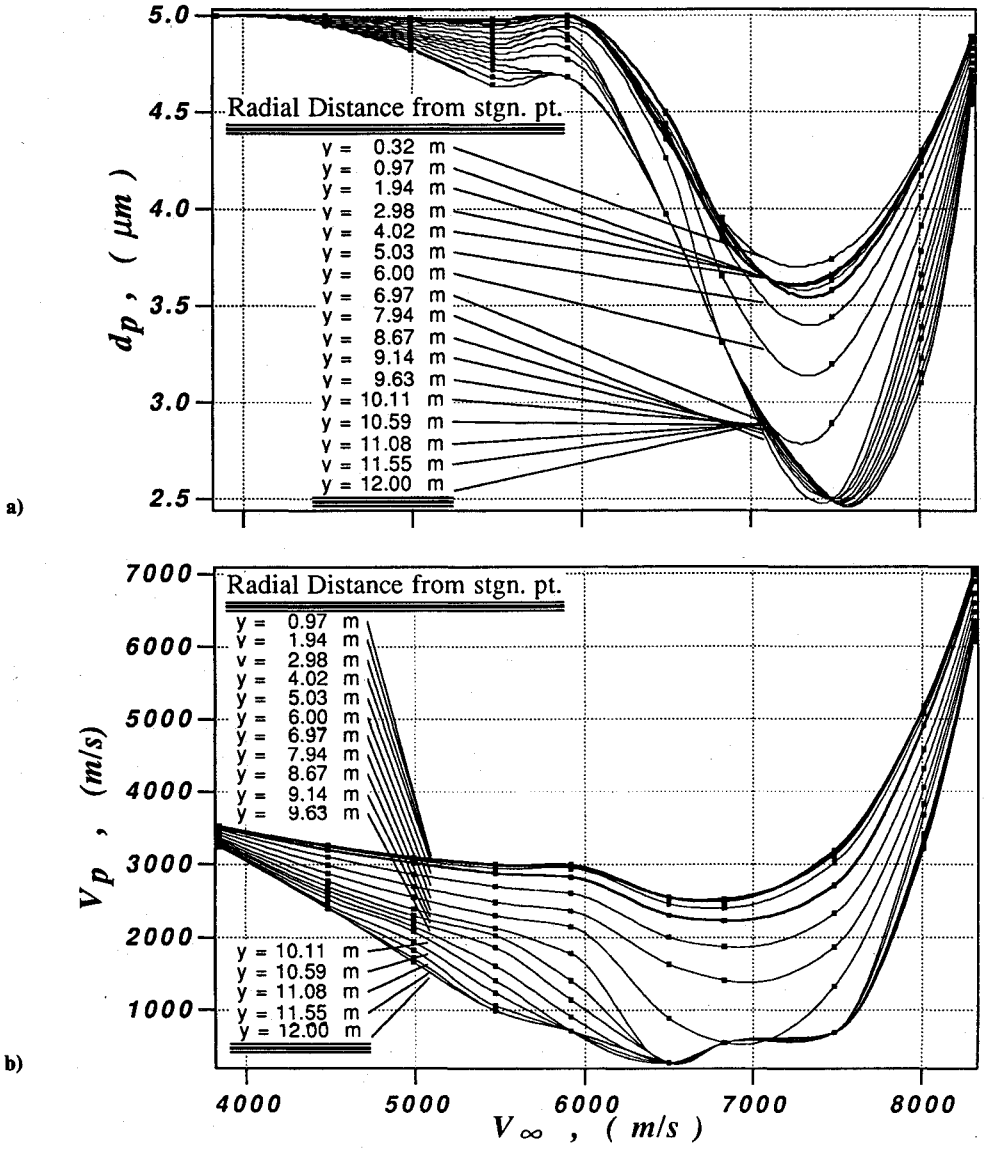

Fig. 8 Particle size and velocity at impact vs flight velocity for $dp_\infty = 5$ and 7 μm: a) particle size at impact for $dp_\infty = 5$ μm and b) particle velocity at impact for $dp_\infty = 5$ μm.

the heat transfer to most of the particles ceases to be large enough to cause significant vaporization. (However, the particles entering the thick shock layer that exists near the vehicle's shoulder can reach their vaporization temperature and continue to shrink at flight speeds down to 5000 m/s. This can occur because the vaporization temperature decreases with decreasing pressure [see Eq. (9)] and the pressure in the shock layer becomes smaller as the flow expands from the stagnation region toward the body's corner.) Data such as those in Fig. 8 are used to compute the extent of surface impact damage over the entire atmospheric trajectory.

Surface Impact Erosion

To determine the surface erosion from particle impacts, the number of dust particles per unit area that enter the shock layer during the entire aerobraking pass must be calculated. This is done using Eq. (16) and noting that, since manned vehicles must fly shallow trajectories to limit the deceleration loads, the summation of forces tangential to the flight path can be approximately written as

$$-m\left(\frac{dV}{dt}\right) \approx \tfrac{1}{2}\rho_\infty V^2 C_D A \qquad (18)$$

Combining Eq. (18) with the kinematic relation $ds = V dt$ and after substituting the result into Eq. (16) and integrating from entry to skip-out velocity yields

$$N = \frac{2(10^{-4})}{\Sigma F_m m_p}\,(m/C_D A)\,\ln(V_E/V_{SK}) \qquad (19)$$

The surface erosion is now computed using the information such as that presented in Fig. 8 and the cratering relations for the appropriate material. For a glassy material, Eqs. (11), (12), and (17) have been combined and are used to arrive at the values that are plotted in Fig. 9. (Note that in Fig. 9 only the curve for $m/C_D A = 200$ kg /m^2 has been calculated precisely. The curves for vehicles with ballistic coefficients of 100 and 300 kg/m^2 are only approximate since the linear $m/C_D A$ scaling based on Eq. (19) was used. In reality, changing the vehicle's ballistic coefficient alters the vehicle's trajectory so that the dust particle heating and deceleration shown in Fig. 8 would also change. However, the latter effect was ignored in Fig. 9). As might be expected, the erosion is greatest at the stagnation point, where the impacts have the highest energy, and declines to almost half at a radial distance of 12 m. The stagnation point region surface erosions range from being 14

c)

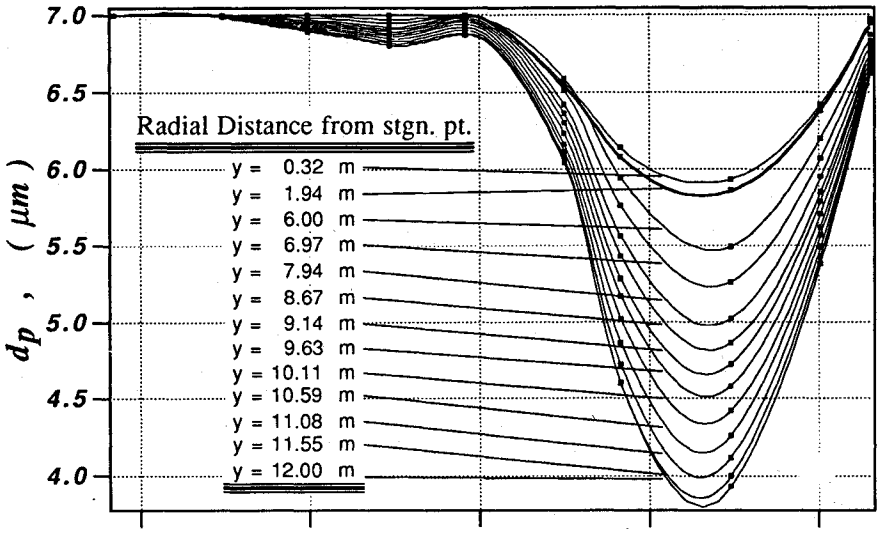

d)

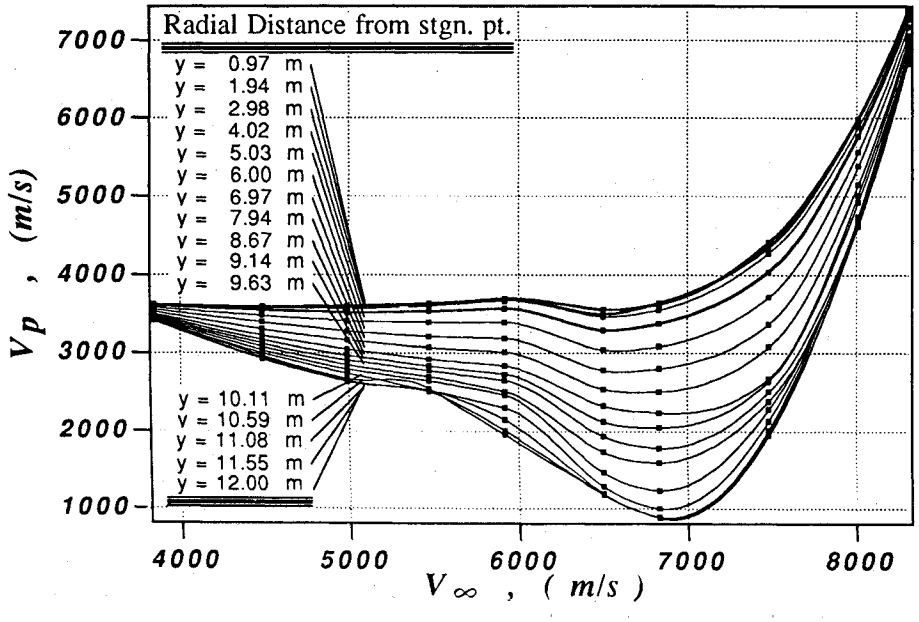

Fig. 8 (cont.) Particle size and velocity at impact vs flight velocity for $dp_\infty = 5$ and 7 μm: c) particle size at impact for $dp_\infty = 7$ μm and d) particle velocity at impact for $dp_\infty = 7$ μm.

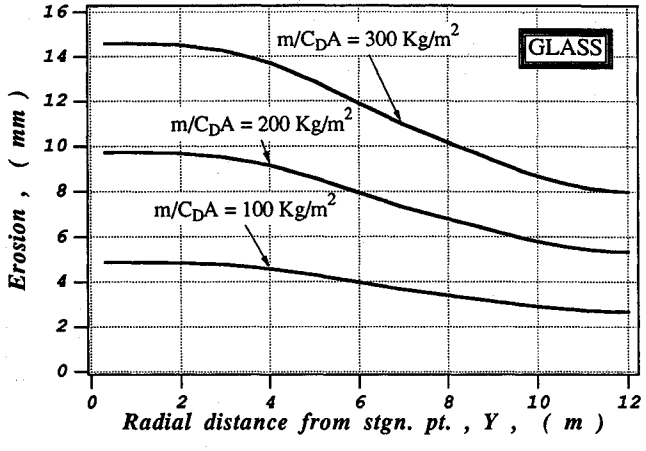

Fig. 9 Surface erosion from dust particle impacts on a glass heatshield.

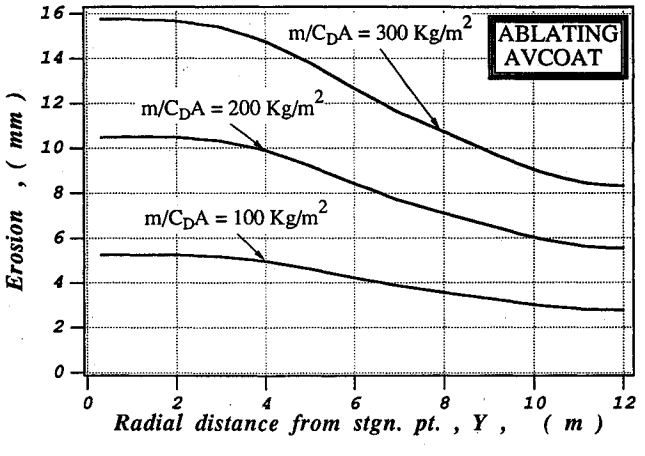

Fig. 10 Surface erosion from dust particle impacts on an AVCOAT heatshield.

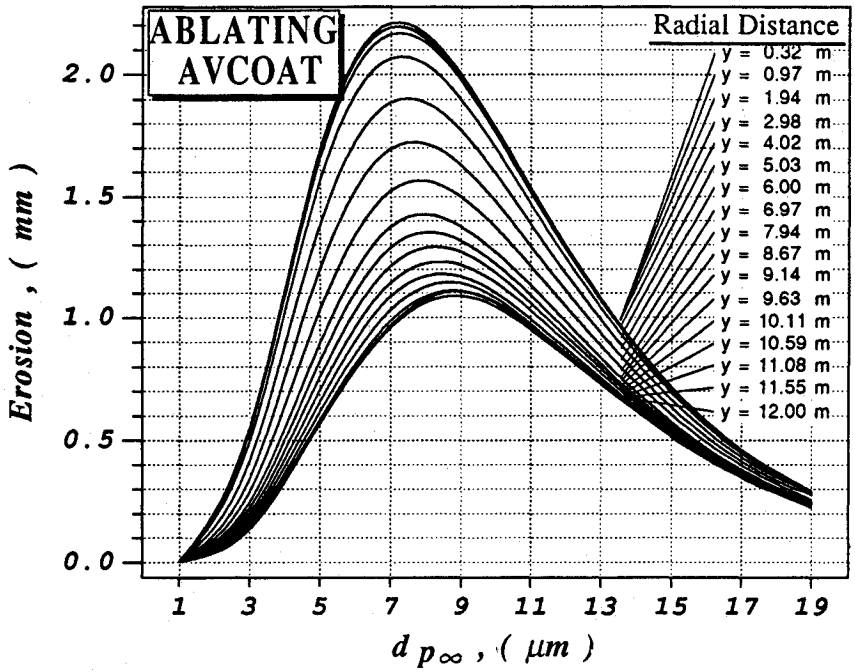

Fig. 11 Erosion distribution as function of initial dust particle diameter (AVCOAT).

to 40 times the thickness of the glassy layer that covers the Shuttle ceramic tiles. If a radiatively cooled heatshield is to be used on the vehicle, then the entire forebody surface requires extra protection. A possible candidate material may be toughened, fibrous insulation (TUFI) being currently developed to protect Shuttle tiles from ice crystal and raindrop impacts. Since no experimental hypervelocity cratering information is available on this new material, it is not yet possible to calculate the thickness or mass required to gain protection from dust particles during Martian aerobraking.

For ablating AVCOAT, Eqs. (14), (15), and (17) have been used to calculate the surface erosion values that are shown in Fig. 10. Both the magnitude of the values and the distribution of erosion with radial distance are similar to the glass surface. Simple inverse density scaling would predict much greater erosion for ablating AVCOAT than for glass. However, the density effect is offset by the extreme brittleness of glass [see Eqs. (11), (12), (14), (15), and (17)]. It is now possible to estimate the additional virgin ablator mass that must be added to the heatshield to withstand entry at 8600 m/s during dust storm conditions. The following additional masses are calculated for vehicles having ballistic coefficients of 100, 200, and 300 kg/m^2, respectively: 950, 1900, and 2850 kg. The heatshielding mass that is removed by erosion is compared with the amount of ablation material required for thermal protection. For example, a forebody thermal protection material mass (for AVCOAT) of 6600 kg was calculated[14] for a Mars aerobraking vehicle of similar size and approximate configuration, using the same entry speed and having a ballistic coefficient of 200 kg/m^2 in a dustless environment. Therefore, the addition of 1900 kg of ablator increases the forebody thermal protection system mass by nearly 29%; however, the total entry vehicle mass is increased by only about 1.3%. Also, the mass of virgin ablator that was needed to account for dust erosion is a conservative value, primarily because the erosion and ablation calculations were performed in an uncoupled manner.

It is also pertinent to estimate the effect that the vehicle's ballistic coefficient and entry velocity have on the extent of surface erosion. First it is assumed that the dust particle impact velocity is proportional to the entry velocity. Second, the assumption is made that vehicles of similar shape and size will have approximately the same fraction of particles that enter the shock layer hitting the vehicle's forebody surface. Therefore, substituting Eqs. (14), (15), and (19) into Eq. (17) leads to the approximate relation

$$\Sigma p \sim (m/C_D A) V_E^2 \ln(V_E/V_{SK}) \tag{20}$$

The approximate linear dependence on the vehicle's ballistic coefficient was established previously in Eq. (19). Note, also, that the surface erosion is approximately proportional to the square of the entry velocity. By using Fig. 9 or 10, depending on the heatshield material, in conjunction with Eq. (20), it is possible to estimate surface erosion on a vehicle of similar size and shape as that used here. However, the present results are not applicable to vehicle configurations having very different shock-layer thicknesses since the deceleration and melting history of the dust particles can vary widely.

Finally, it is important to determine which size particles cause the most erosion of an ablating surface. Although small particles are most abundant, many do not reach the heatshield or hit at modest velocities (Fig. 8). In contrast, large particles are not decelerated much in the shock layer but account for only a small fraction of the total number. In Fig. 11, the contributions to the erosion of the ablating AVCOAT surface are shown for the range of particle sizes considered. Note that much of the erosion is caused by particles ranging in initial size from 4 to 15 μm, with the most severe damage coming from those that are 7 to 9 μm in diameter. Therefore, it is recommended that aeronomy experiments be made during future Mars missions to determine the lifetime of dust particles in the aforementioned size range at altitudes in the neighborhood of 40 km and following major dust storms.

Concluding Remarks

The effects of dust particle impacts on the erosion of two different kinds of heatshielding materials were calculated for a 26 m diam aerobraking vehicle entering the Mars atmosphere at 8600 m/s. The approximately 2–4% probability of encountering dust storm activity on arrival at the planet requires that the vehicle's heatshield be designed for these conditions. An explicit, thin-layer, Navier-Stokes code was used to compute the dustless flowfield about the vehicle for the actual Martian atmospheric composition. The deceleration and melting of the dust particles within the forebody shock layer were computed for dust spherules having initial diameters from 1 to 19 μm. Although all particles considered began vaporizing shortly after entering the shock layer, most survived to hit the heat-

shield surface. Two different forebody heatshield materials were considered. The first consisted of Shuttle ceramic tiles with glassy surfaces, and the second was a medium-density ablator known as AVCOAT-5026. For the blunt-cone configuration that was considered here, the surface erosion peaked at the stagnation point and declined to nearly half the stagnation point values at a radial distance of 12 m. For example, a vehicle with a ballistic coefficient of 200 kg/m^2 and a glassy heatshield surface experienced an average of 7 mm of surface erosion, or about 20 times the thickness of the black glassy layer on ceramic tiles. The same vehicle using AVCOAT ablator experienced similar amounts of erosion. An additional 1900 kg of virgin AVCOAT was required to protect the vehicle during an 8600 m/s entry aerocapture maneuver in a dust-laden atmosphere. However, the additional mass of virgin ablator that was needed to account for dust erosion is a conservative value since the erosion and ablation calculations were performed in an uncoupled manner. The resulting increase in the forebody thermal protection mass was 29%, or about 1.3% of the vehicle's mass. Although additional heatshielding material must be provided for protection when entering a dust-laden atmosphere, the mass penalty does not compromise the use of aerobraking at Mars.

An approximate scaling law was derived for dust-caused heatshield surface erosion. The scaling relation predicts that for a given vehicle size and shape the erosion is, to first order, directly proportional to the vehicle's m/C_DA and to the square of the entry velocity.

Lastly, it was found that particles having initial diameters of 7 to 9 μm cause the most damage. It is recommended that future Mars aeronomy missions attempt to measure the lifetimes of these large dust particles at high altitudes, near 40 km, following major dust storms.

Acknowledgments

The authors thank the following of their colleagues at NASA Ames Research Center for valuable assistance and discussions: Grant Palmer, Ethiraj Venkatapathy, William Henline, and Dinesh Prabhu.

References

[1]Syvertson, C. A., and Dennis, D. H., "Trends in High-Speed Atmospheric Flight," AIAA Paper 64-514, July 1964.

[2]Tauber, M. E., and Seiff, A., "Optimization Analysis of Heating of Conical Bodies Making Lifting Hyperbolic Entries into the Atmospheres of Earth and Mars," *Proceedings of the AIAA Entry Technology Conference* (Williamsburg, VA), AIAA Conference Publication-9, AIAA, New York, Oct. 1964.

[3]Clark, B., "Manned Mars Missions for the Year 2000," AIAA Paper 89-0512, Jan. 1989.

[4]Braun, R. D., and Blersch, D. J., "Propulsive Options for a Manned Mars Transportation System," AIAA Paper 89-2950, Jan. 1989.

[5]Clark, B., Geels, S., Sutter, B., Zaveri, R., and Zubrin, R., "Advanced Technologies for Nuclear Propulsion," AIAA Paper 91-3012, July 1991.

[6]Appleby, M. H., Tanner, E. R., II, Nealy, J. E., Ryder, S. P., and Pike, E. L., "Practical Response to Radiation Assessment for Spacecraft Design," AIAA Paper 91-0425, Jan. 1991.

[7]Seiff, A., and Kirk, D. B., "Structure of the Atmosphere of Mars in Summer at Mid-Latitudes," *Journal of Geophysical Research,* Vol. 82, No. 8, 1977, pp. 4364–4378.

[8]Owen, T., Biemann, K., Rushneck, D. R, Biller, J. E., Howarth, D. W., and LaFleur, A. L., "The Composition of the Atmosphere at the Surface of Mars," *Journal of Geophysical Research,* Vol. 82, No. 8, 1977, pp. 4633–4639.

[9]Pollack, J. B., Colburn, D. S., Flasar, F. M., and Kahn, R., Carlston, C. E., and Pidek, D., "Properties and Effects of Dust Particles Suspended in the Martian Atmosphere," *Journal of Geophysical Research,* Vol. 84, No. B6, June 1979, pp. 2929–2945.

[10]Toon, O. W., Pollack, J. B., and Sagan, C., "Physical Properties of the Particles Composing the Martian Dust Storm of 1971–1972," *Icarus,* Vol. 30, No. 4, 1977, pp. 663–696.

[11]Conrath, B. J., "Thermal Structure of the Martian Atmosphere During the Dissipation of the Dust Storm of 1971," *Icarus,* Vol. 24, No. 1, Jan. 1975, pp. 36–43.

[12]Anderson, E., and Leovy, C., "Mariner 9 Television Limb Observations of Dust and Ice Hazes on Mars," *Journal of Atmospheric Science,* Vol., 35, No. 4, 1978, pp. 723–734.

[13]Tauber, M. E., Bowles, J. V., and Yang, L., "The Use of Atmospheric Braking During Mars Missions," *Journal of Spacecraft and Rockets,* Vol. 27, No. 5, 1990, pp. 514–521.

[14]Tauber, M., Chargin, M., Henline, W., Chiu, A., Yang, L., Hamm, K. R., Jr., and Miura, H., "Aerobrake Design Studies for Manned Mars Missions," AIAA Paper 91-1344, June 1991.

[15]Lyne, J. E., Anagnost, A., and Tauber, M. E., "A Parametric Study of Manned Aerocapture at Mars," AIAA Paper 91-2871, Aug. 1991.

[16]Papadopoulos, P., Tauber, M. E., and Chang, I. D., "Aerobraking in a Dusty Martian Atmosphere," AIAA Paper 90-1700, June 1990.

[17]Haberle, R. M., "Interannual Variability of Global Dust Storms on Mars," *Science,* Vol. 234, Oct. 1986, pp. 459–461.

[18]Zurek, R. W., "Martian Great Dust Storms: An Update," *Icarus,* Vol. 50, No. 2/3, 1982, pp. 288–310.

[19]Murphy, J. R., Toon, O. B., Haberle, R. M., and Pollack, J. B., "Numerical Simulations of the Decay of Martian Global Dust Storms," *Journal of Geophysical Research,* Vol. 95, No. B9, Aug. 1990, pp. 14629–14648.

[20]Palmer, G., "An Improved Flux-Split Algorithm Applied to Hypersonic Flows in Chemical Equilibrium," AIAA Paper 88-2693, June 1988.

[21]Gordon, S., and McBride, B. J., "Computer Program for Calculation of Complex Chemical Equilibrium Compositions, Rocket Performance, Incident and Reflected Shocks, and Chapman-Jouget Detonations," NASA SP-273, Interim Revision, March 1976.

[22]Davies, C., and Venkatapathy, E., "A Simplified Self-Adaptive Grid Method, SAGE," NASA TM 102198, Oct. 1989.

[23]Waldman, G. D., and Reinecke, W. G., "Particle Trajectories, Heating, and Breakup in Hypersonic Shock Layers," *AIAA Journal,* Vol. 9, No. 6, June 1971, pp. 1040–1048.

[24]Henderson, C. B., "Drag Coefficients of Spheres in Continuum and Rarefied Flows," *AIAA Journal,* Vol. 14, No. 6, 1976, pp. 600–602.

[25]Schaff, S. A., and Chambre, P. L., *Flow of Rarefied Gases,* Princeton Univ. Press, Princeton, NJ, 1961.

[26]Eckert, E. R. G., and Drake, R. M., Jr., *Heat and Mass Transfer,* McGraw-Hill, New York, 1959.

[27]Springer, G., "Heat Transfer in Rarefied Gases," *9th International Symposium on Rarefied Gas Dynamics,* edited by M. Becker and M. Fiebig, DFVLR Press, Goettingen, Germany, 1974, pp. 163–218.

[28]Incorpera, F. P., and Dewitt, D. P., *Fundamentals of Heat Transfer,* Wiley, New York, 1981.

[29]Centolanzi, F., and Chapman, D., "Vapor Pressure of Tektite Glass and its Bearing on Tektite Trajectories Determined from Aerodynamic Analysis," *Journal of Geophysical Research,* Vol. 71, No. 6, 1966, pp. 1735–1749.

[30]Baldwin, B., and Sheaffer, Y., "Ablation and Breakup of Large Meteoroids During Atmospheric Entry," *Journal of Geophysical Research,* Vol. 76, No. 19, 1971, pp. 4653–4668.

[31]Denardo, B. P., and Nysmith, C. R., "Momentum Transfer and Cratering Phenomena Associated with the Impact of Aluminum Spheres into Thick Aluminum Targets at Velocities to 24,000 Feet Per Second," NASA TM X-54,046, April 1964.

[32]Lorentz, G. C., "Simulation of the Erosive Effects of Multiple Particle Impacts in Hypersonic Flow," *Journal of Spacecraft and Rockets,* Vol. 7, No. 2, 1970, pp. 119–125.

[33]McMillen, L. D., Dunbar, L. E., and Jackson, D., "Heatshield Material Erosion at Hypersonic Velocities," AIAA Paper 76-321, July 1976.

[34]Flaherty, R., "Impact Characteristics in Fused Silica for Various Projectile Velocities," *Journal of Spacecraft and Rockets,* Vol. 7, No. 3, 1970, pp. 319–324.

[35]Gault, D., "Impact Cratering," *A Primer in Lunar Geology,* edited by R. Greely and P. Schultz, NASA TM-62,359, July 1974.

[36]Cour-Palais, B. G., "Hypervelocity Impact Investigations and Meteoroid Shielding Experience Related to Apollo and Skylab," *Orbital Debris,* edited by D. J. Kessler and S. Y. Su, NASA Conf. Publication 2360, 1985, pp. 247–274.

[37]Clever, R. M., and Denny, V. E., "Response of Charring Ablators to Severe Aerodynamic and Erosion Environments," *Journal of Spacecraft and Rockets,* Vol. 12, No. 9, 1975, pp. 558–564.

Gerald T. Chrusciel
Associate Editor